Chemistry
A European
Journal

Chemistry Europe
European Chemical Societies Publishing

Accepted Article

Title: Large-Amplitude Thermal Vibration-Coupled Valence Tautomeric Transition Observed in a Conductive One-Dimensional Rhodium–Dioxolene Complex

Authors: Minoru Mitsumi, Yuuki Komatsu, Masahiro Hashimoto, Koshiro Toriumi, Yasutaka Kitagawa, Yuji Miyazaki, Hiroki Akutsu, and Haruo Akashi

To be cited as: *Chem. Eur. J.* 10.1002/chem.202004217

Link to VoR: https://doi.org/10.1002/chem.202004217

WILEY-VCH

10.1002/chem.202004217

WILEY-VCH

FULL PAPER

Large-Amplitude Thermal Vibration-Coupled Valence Tautomeric Transition Observed in a Conductive One-Dimensional Rhodium–Dioxolene Complex

Minoru Mitsumi,*[a] Yuuki Komatsu,[b] Masahiro Hashimoto,[b] Koshiro Toriumi,[b] Yasutaka Kitagawa,*[c] Yuji Miyazaki,*[d] Hiroki Akutsu,[e] and Haruo Akashi[f]

Dedicated to the memory of Professor Gleb A. Abakumov, who passed away on August 29, 2019.

[a] Prof. M. Mitsumi
Department of Chemistry, Faculty of Science, Okayama University of Science
1-1 Ridai-cho, Kita-ku, Okayama 700-0005 (Japan)
E-mail: mitsumi@chem.ous.ac.jp
[b] Y. Komatsu, M. Hashimoto, Prof. Koshiro Toriumi
Department of Material Science, Graduate School of Material Science, University of Hyogo
3-2-1 Kouto, Kamigori-cho, Ako-gun, Hyogo 678-1297 (Japan)
[c] Prof. Y. Kitagawa
Department of Materials Engineering Science, Graduate School of Engineering Science, Osaka University
1-3 Machikaneyama, Toyonaka, Osaka 560-8531 (Japan)
E-mail: kitagawa@cheng.es.osaka-u.ac.jp
[d] Prof. Yuji Miyazaki
Research Center for Thermal and Entropic Science, Graduate School of Science, Osaka University
1-1 Machikaneyama, Toyonaka, Osaka 560-0043 (Japan)
E-mail: miyazaki@chem.sci.osaka-u.ac.jp
[e] Prof. H. Akutsu
Department of Chemistry, Graduate School of Science, Osaka University
1-1 Machikaneyama, Toyonaka, Osaka 560-0043 (Japan)
[f] Prof. H. Akashi
Research Institute of Natural Sciences, Okayama University of Science
1-1 Ridai-cho, Kita-ku, Okayama 700-0005 (Japan)

Supporting information for this article is given via a link at the end of the document.

Abstract: The exploration of dynamic molecular crystals is a fascinating theme for materials scientists owing to their fundamental science and potential application to molecular devices. Herein, we report a one-dimensional (1D) rhodium–dioxolene complex that exhibits drastic changes in properties with the phase transition. The X-ray photoelectron spectroscopy (XPS) reveals that the room-temperature (RT) phase is in a mixed-valence state, and therefore, the drastic changes originate from the mixed-valence state appearing in the RT phase. Another notable feature is that the mean square displacements of the rhodium atoms along the 1D chain dramatically increase in the RT phase, indicating a large-amplitude vibration of the Rh–Rh bonds. From these results, we propose a possible mechanism for the appearance of the mixed-valence state in the RT phase based on the thermal electron transfer from the 1D d-band to the semiquinonato π* orbital coupled with the large-amplitude vibration of the Rh–Rh bonds.

Introduction

The development of bistable molecular materials that can control their physical properties, such as their electronic, magnetic, and optical properties, by external stimuli, such as heat, light, pressure, electric or magnetic fields, has received increased attention owing to their promising applications in molecular switches, molecular memories, sensors, and so on.[1] These switchable physical properties originate from the interconversion between two nearly degenerated electronic states caused by charge transfer,[2] spin transition,[1b,3] charge-transfer coupled spin transitions,[4] proton transfer,[5] and cooperative proton–electron transfer[6] that occur in response to external stimuli. In addition, the switching that originates from the motion of constituted atoms or molecules in molecular materials has also attracted attention in recent years.[7] Such stimuli-responsive, bistable crystalline molecular materials are summarized in a recent review by Sato as dynamic molecular crystals.[1d] Valence tautomeric (VT) complexes derived from redox-active ligands and metal centers, represented by metal–dioxolene complexes, can take two valence isomers or redox isomers with different localized electronic structures exhibiting different physical properties.[8] VT transitions between these isomers accompanying intramolecular electron transfer can not only cause changes in the valence and spin states and radical formation and disappearance but also lead to interesting mixed-valence states[9] and spin transitions,[2a-c,10] and these features can be tuned by controlling the VT transitions by external stimuli, such as heat,[10a,10f,10g,11] light,[1g,10e,10f,12] X-ray,[13] pressure,[3g]

10.1002/chem.202004217

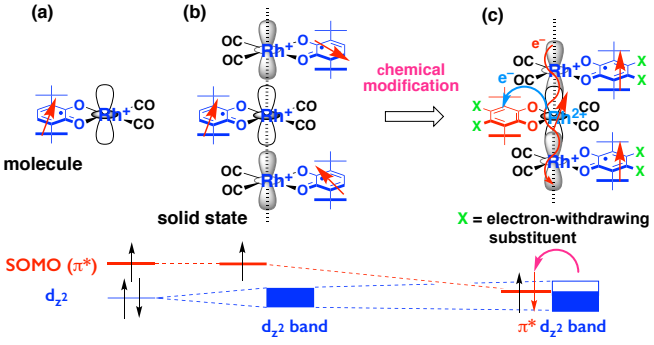

Scheme 1. Illustration of the frontier orbital control and energy level diagrams of 1D rhodium–dioxolene complexes

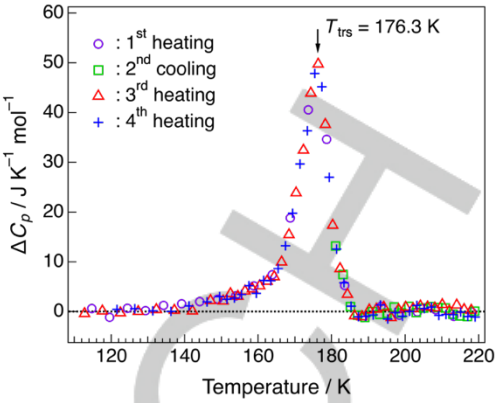

Figure 1. Excess heat capacity of [Rh(3,6-DBDiox-4-NO$_2$)(CO)$_2$]$_\infty$ (**4**) as a function of temperature. The measurements in the transition region were repeated four times to determine the accurate transition temperature.

electric[14] and magnetic fields.[15] Therefore, VT transitions are widely utilized as stimuli-responsive, controllable functions on dynamic molecular crystals.

To realize multifunctional molecular materials that can control both electrical and magnetic properties by utilizing the VT transition, frontier orbital control is conducted for a one-dimensional (1D) rhodium(I)–semiquinonato complex [Rh(3,6-DBSQ)(CO)$_2$]$_\infty$ (**1**; 3,6-DBSQ$^{\bullet-}$ = 3,6-di-*tert*-butyl-1,2-benzosemiquinonato) by chemical modification.[16] Semiquinonate is an organic radical anion and is one of the redox series of dioxolene, which can produce three different redox isomers, i.e., benzoquinone (BQ), semiquinonate (SQ$^{\bullet-}$), and catecholate (Cat^{2-}), via two sequential one-electron transfers. In our target system, the semiquinonato radical can serve not only as a spin carrier of S = ½ but also as an electron acceptor for the partial oxidation of a rhodium(I) linear chain. Thus, the linear rhodium chain can produce the 1D conducting d-band via electron transfer from the rhodium(I) ion to the semiquinonato ligand (valence tautomerism), i.e., the partial oxidation of the rhodium linear chain. In addition, the filling of the 1D d-band can be tuned post-synthetically in cases where the application of external stimuli, such as heat, light, or pressure, can control valence tautomerism. The low-lying π* orbitals of the 3,6-DBSQ$^{\bullet-}$ ligand are relatively close in energy to the upper level of the filled 1D d-band derived from electron-rich rhodium(I) ions, which facilitates electron transfer from the rhodium(I) ion to the 3,6-DBSQ$^{\bullet-}$ ligand by chemical modification. In a previously reported 1D mixed-valence rhodium(I,II)–semiquinonato/catecholato complex [Rh(3,6-DBDiox-4,5-Cl$_2$)(CO)$_2$]$_\infty$ (**2**), where 3,6-DBDiox-4,5-Cl$_2$ indicates 3,6-di-*tert*-butyl-4,5-dichloro-1,2-benzosemiquinonato or 3,6-di-*tert*-butyl-4,5-dichlorocatecholato, electron transfer from the rhodium(I) ion to the semiquinonato ligand was realized in the solid state by introducing two chloro substituents into the 4 and 5 positions of the 3,6-DBSQ$^{\bullet-}$ ligand.[9a] The average formal oxidation state of the rhodium ion is +1.33, and the compound is a paramagnetic semiconductor with a significantly higher electrical conductivity of σ_{RT} = 17–34 S cm^{-1} at RT. However, the band-filling control of **2** through the valence tautomerism by the temperature could not be realized post-synthetically. On the other hand, we have also found that the introduction of two methoxy groups at the 4 and 5 positions of the 3,6-DBSQ$^{\bullet-}$ ligand has led to intriguing bistable multifunctionality and switchable very strong ferromagnetic-to-antiferromagnetic coupling of the 1D rhodium(I)–semiquinonato complex, [Rh(3,6-DBSQ-4,5-(MeO)$_2$)(CO)$_2$]$_\infty$ (**3**; 3,6-DBSQ-4,5-(MeO)$_2^{\bullet-}$ = 3,6-di-*tert*-butyl-4,5-dimethoxy-1,2-benzosemiquinonato), although the basic skeletons of the Rh(3,6-DBSQ)(CO)$_2$ moieties are almost the same among compounds **1**–**3**.[10d]

Herein, we report the synthesis, crystal structure, and solid-state properties of a conductive 1D rhodium–dioxolene complex, [Rh(3,6-DBDiox-4-NO$_2$)]$_\infty$ (**4**), that exhibits drastic changes in the solid-state properties with a first-order phase transition at 176.3 K. In particular, the conducting behavior shows typical semiconducting behavior in the low-temperature (LT) phase but drastically changes to a relatively high electrical conductivity with little temperature dependence in the room-temperature (RT) phase. The X-ray photoelectron spectroscopy (XPS) spectrum indicated that compound **4** in the RT phase exists in a Rh(I,II) mixed-valence state due to valence tautomerism. The temperature dependence of the X-ray crystal structures indicated that the mean square displacements of the rhodium atoms along the 1D chain dramatically increase in the RT phase, indicating the occurrence of a large-amplitude vibration of the Rh–Rh bonds in the RT phase. We performed density functional theory (DFT) calculations to estimate the energy levels of the semiquinonato π* orbital and 1D d-band. Finally, employing a combination of these results, we propose a possible mechanism for the appearance of the mixed-valence state in the RT phase from the viewpoint of thermal electron transfer from the filled 1D d-band to the vacant semiquinonato π* orbital coupled with the increase in the band dispersion accompanying the large-amplitude vibration of the Rh–Rh bonds.

Results and Discussion

Synthesis and heat capacity

Dark brown needle crystals of compound **4** were prepared by a redox reaction of [Rh$_4$(CO)$_{12}$] with 3,6-di-*tert*-butyl-4-nitro-1,2-benzoquinone (3,6-DBBQ-4-NO$_2$) in a mixture of hexane–toluene (3:1, v/v). To examine whether the compound **4** undergoes a phase transition, the heat capacity was measured from 7 K to 302 K by adiabatic calorimetry (Figure 1). A thermal anomaly was observed at T_{trs} = 176.3 K during heating, indicating the existence of RT and LT phases. The enthalpy and entropy of the phase transition were determined to be 580(16) J mol^{-1} and 3.39(11) J K^{-1} mol^{-1}, respectively. Generally, the transition entropy for the

10.1002/chem.202004217

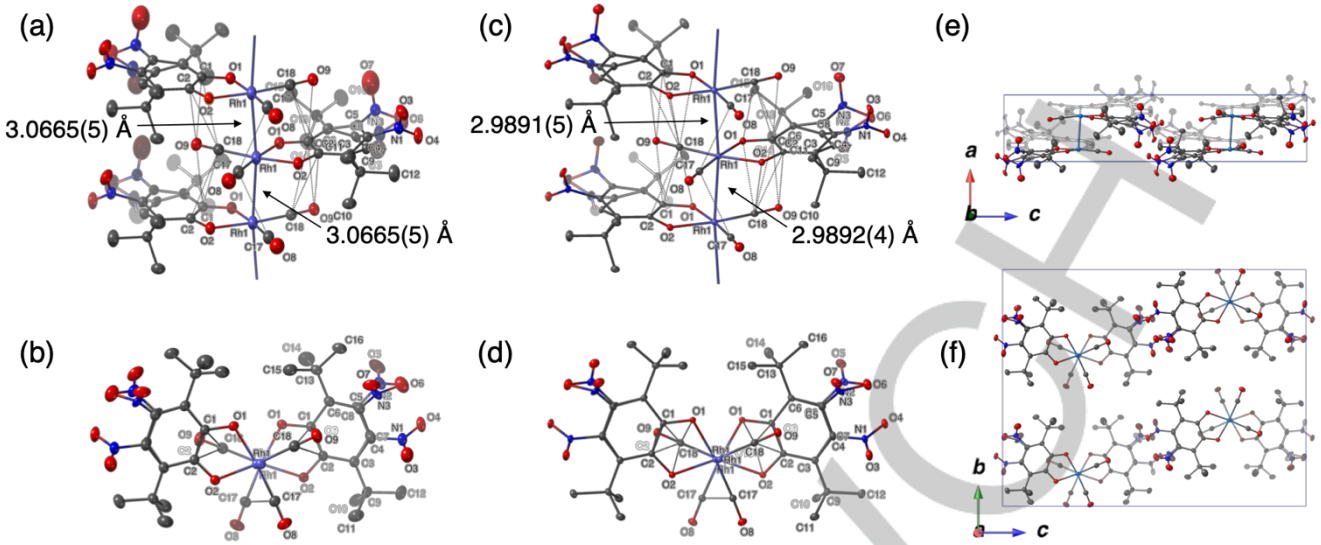

Figure 2. Crystal structure of $[Rh(3,6\text{-DBDiox-4-NO}_2)(CO)_2]_\infty$ (**4**). a) Structure of the infinite chain built from a stack of planar complex molecules, and b) structural view down the 1D chain showing an overlap mode of the complex molecules in the RT phase (288 K). c) Structure of an infinite chain, and d) structural view down the 1D chain in the LT phase (101 K). Thermal ellipsoids are drawn at the 25 % probability level. Intermolecular C···O and C···C contacts shorter than the sum of the van der Waals radii of the contacting atoms are represented by dashed lines. e) Packing diagram viewed down the *b*-axis, and f) packing diagram viewed down the *a*-axis in the LT phase (101 K). Thermal ellipsoids are drawn at the 50 % probability level.

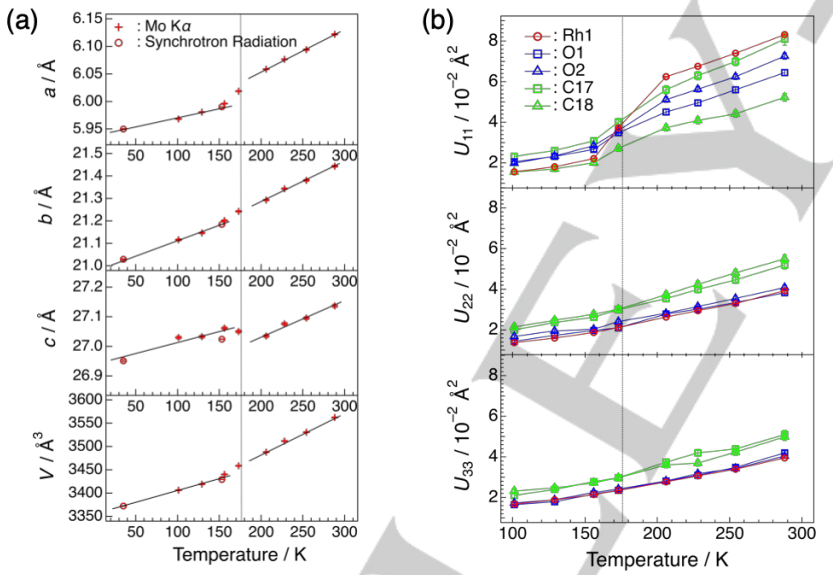

Figure 3. a) Temperature dependence of the lattice parameters of $[Rh(3,6\text{-DBDiox-4-NO}_2)(CO)_2]_\infty$ (**4**). The *a*-axis is parallel to the 1D chain direction. The dashed line represents the phase transition temperature. b) Temperature dependence of the anisotropic atomic displacement parameters (ADPs; U_{11}, U_{22}, and U_{33}) of the rhodium atom and the coordinated oxygen atoms of the semiquinonato ligand and carbon atoms of the carbonyl ligands in **4**.

order–disorder-type phase transition is known to be a large value, such as $\Delta_{trs}S = R \ln 2 = 5.76$ J K^{-1} mol^{-1}. Therefore, since the observed transition entropy is smaller than 5.76 J K^{-1} mol^{-1}, this phase transition is presumably not of the order–disorder type. However, the value is somewhat larger than that for the typical displacive type phase transition.[17] This cause will be discussed later.

X-ray crystal structure analyses

To investigate the details of the temperature dependence of the crystal structure, the crystal structures of compound **4** were determined at ten different temperatures from 288 K to 35 K by single-crystal X-ray crystal structure analyses. Crystallographic data and intensity data collection for all structures are provided in the Supporting Information (Table S1). The 1D chain structures and packing diagrams in the RT and LT phases are shown in Figure 2 and Figures S1, S2 in Supporting Information, respectively. Although compound **4** undergoes a first-order phase transition, all the structures determined at each temperature belong to the same orthorhombic space group *Pbca* and the asymmetric unit composed of only one complex molecule.

First, we describe the crystal structure of **4** at 288 K in the RT phase (Figure 2a,b). The crystal structure is composed of neutral 1D chains of the planar complex molecule stacked in equal intervals with a staggered arrangement along the *a*-axis, where the twisting angles between adjacent molecules estimated from the torsion angles of O1–Rh1–Rh1*–O2* and O2–Rh1–Rh1*–O1* are approximately 139° at 288 K. The Rh1–Rh1* distance at 288 K is 3.0665(5) Å. Regarding the intermolecular contacts in the 1D chain, the intermolecular C···O contacts (3.079(4)–3.104(4) Å) and C···C contacts (3.156(5)–3.377(5) Å) shorter than the sum of the van der Waals radii of contacting atoms exist between the dioxolene ligand and carbonyl ligand in the adjacent stacked molecules; they are represented by dashed lines in Figure 2a,b. The slight zigzag conformation is observed in the Rh–Rh chain, and the bond angle of Rh1'–Rh1–Rh1* is 173.108(19)°. This result is due to the influence of these strong intermolecular interactions. The positional disorder in the dioxolene moiety was observed as follows (Figure S3 in Supporting Information). The carbon atoms in the 4- and 5-positions of the dioxolene ring are disordered in both the upper and lower positions of the molecular plane, and their occupancy factors were estimated to be 0.65 (C4, C5) and 0.35 (C7, C8), respectively. Moreover, the nitro group binding to these carbon

atoms is disordered over three sites with estimated occupancy factors of 0.55 (N1), 0.10 (N3) and 0.35 (N2). This disorder model was applied to all other temperature data sets. On the other hand, the Rh1–Rh1* distance at 101 K in the LT phase is 2.9892(4) Å, which is shortened by 0.077 Å compared to 288 K (Figure 2c,d). The bond angle of Rh1'–Rh1–Rh1* is 173.371(16)°, which is very slightly increased compared with that in the RT phase. The intermolecular C···O contacts (2.980(4)–3.205(4) Å) and C···C contacts (3.085(4)–3.307(4) Å) between dioxolene ligands and carbonyl ligands in the adjacent stacked molecules are also slightly shortened compared with those in the RT phase (Figure 2c,d).

The temperature dependence of the lattice parameters and Rh–Rh distance of **4** are shown in Figure 3a and Figure S4 in Supporting Information, respectively. In accordance with the thermal anomaly observed in the heat capacity, the slope of each lattice parameter has changed in the vicinity of 175 K. While the *a*-axis parallel to the 1D Rh chain has elongated with the phase transition, the *c*-axis has contracted. The Rh1–Rh1* distance at 288 K is 3.0665(5) Å, which is 0.21 Å shorter than that of [Rh^{I}(3,6-DBSQ)(CO)$_2$]$_\infty$ (**1**) (3.252(4) and 3.304(5) Å at 294−297 K)[16a] but 0.19 Å longer than that of [Rh^{I,II}(3,6-DBDiox-4,5-Cl$_2$)(CO)$_2$]$_\infty$ (**2**) (2.8629(2)−2.8984(3) Å at 302 K) on average.[9a] Formally, there is no bond between Rh atoms in the 1D Rh(I) chain because the d_{z^2} orbital involved in the bond is filled by two electrons. However, when the rhodium atom is partially oxidized, the Rh–Rh distance decreases owing to bond formation by removing the electrons from the antibonding orbitals of the 1D Rh(I) chain. The shorter Rh–Rh distance compared to that of a typical Rh(I)–semiquinonato complex suggests the possibility that a slight amount of charge transfer from the Rh(I) ion to semiquinonato ligand has occurred to produce a Rh(I,II)–semiquinonato/catecholato mixed-valence state. The space group in the LT phase is also *Pbca*, which is the same as the RT phase, and no indication of lattice distortion, such as dimerization due to the phase transition, was observed. However, a drastic increase in the Rh–Rh distance (approximately 0.031 Å) is observed in the vicinity of 175 K due to the phase transition.

The temperature dependence of the anisotropic atomic displacement parameters (ADPs; U_{11}, U_{22}, and U_{33}) of the rhodium atom and the coordinated oxygen atoms of the dioxolene ligand and carbon atoms of carbonyl ligands in **4** is shown in Figure 3b. U_{11}, U_{22}, and U_{33} indicate the squares of the average moving distance of the atom along the *a*-, *b*-, and *c*-axes from its equilibrium position, respectively. For U_{11} corresponding to the 1D chain direction, a drastic increase in all atoms was observed in the vicinity of the transition point. In particular, the U_{11} of the rhodium atom is remarkably increased by approximately 0.04 Å^2 with the phase transition. However, U_{22} and U_{33} in the direction perpendicular to the 1D chain increase almost linearly with increasing temperature. For the cause of the drastic increase in the temperature factor, either static structural disorder or dynamic disorder of atoms may be considered. The observed increase in U_{11} is attributed to the increase in the amplitude of the thermal vibration since it occurs not in the LT phase but starts in the RT phase where lattice distortion is generally eliminated. Therefore, it is suggested that rhodium atoms in the RT phase vibrate with a large amplitude along the 1D chain direction. Since the rates of increase in U_{11} of the coordinated oxygen and carbon atoms are smaller than that of the rhodium atom, it is considered that these atoms are dragged by the large-amplitude vibration of the rhodium atoms and vibrate greatly along the 1D chain direction.

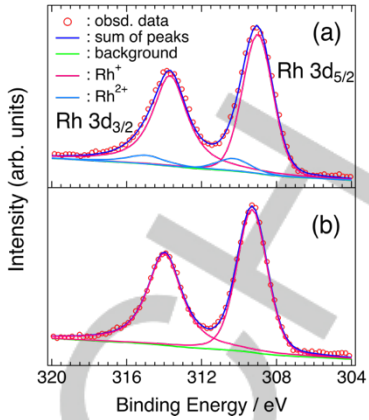

Figure 4. Rh 3d$_{5/2}$ and 3d$_{3/2}$ core-level spectra for a) [Rh(3,6-DBDiox-4-NO$_2$)(CO)$_2$]$_\infty$ (**4**) and b) [Rh^{I}(3,6-DBSQ)(CO)$_2$]$_\infty$ (**1**). The solid lines are the deconvoluted components and the sum of all the components.

Table 1. XPS Data for [Rh^{I}(3,6-DBSQ)(CO)$_2$]$_\infty$ (**1**) and [Rh(3,6-DBDiox-4-NO$_2$)(CO)$_2$]$_\infty$ (**4**)

	binding energies, eV[a,b]			
compound	Rh$^+$ 3d$_{5/2}$	Rh^{2+} 3d$_{5/2}$	Rh$^+$ 3d$_{3/2}$	Rh^{2+} 3d$_{3/2}$
1	309.31 (1.91)		313.99 (2.17)	
4	308.94 (2.00)		314.88 (2.48)	
4	309.17 (1.91)	310.49 (2.12)	313.86 (2.17)	315.18 (2.41)

[a] Full width at half maximum (fwhm) values for peaks are given in parentheses. [b] These values were corrected against the C1s peak using a value of 284.6 eV

To discuss the lattice periodicity of the 1D chain in each phase, X-ray diffraction photographs of **4** were taken in the LT and RT phases (Figure S5 in Supporting Information). The X-ray diffraction pattern in the RT phase exhibits diffuse lines at 0.5*a**, in addition to the main Bragg reflections, indicating that a new periodic ordering along the *a*-axis (1D chain direction) with a 2-fold repetition length of the *a*-axis has occurred in the RT phase. Considering the large-amplitude vibration that appears only at the RT phase, the observed diffuse scattering can be attributed to dynamic distortion of the rhodium atoms. From these results, as the possible phonon mode expected in the RT phase, we propose phonon mode 2, which satisfies the two-fold periodicity (see Figure S6c in Supporting Information).

X-ray photoelectron spectroscopy (XPS)

To examine the valence state of the rhodium ions, we measured the XPS spectrum of **4** at RT together with that of [Rh^{I}(3,6-DBSQ)(CO)$_2$]$_\infty$ (**1**) (Figure 4 and Table 1). Rh(I)–semiquinonato complex **1** shows sharp Rh 3d$_{5/2}$ and 3d$_{3/2}$ peaks, whereas the full width at half maximum (fwhm) values of the Rh 3d$_{5/2}$ and 3d$_{3/2}$ peaks of compound **4** are slightly larger than those of **1**. When the curve deconvolution using a Gaussian–Lorentzian line shape fit is performed by assuming compound **4** to be in the mixed-valence state composed of Rh(I) and Rh(II), these peaks could be resolved into two sets of Rh$^+$ 3d$_{5/2,3/2}$ and Rh^{2+} 3d$_{5/2,3/2}$ doublets. The peak area ratio of the Rh$^+$ 3d$_{5/2}$/Rh^{2+} 3d$_{5/2}$ and Rh$^+$ 3d$_{3/2}$/Rh^{2+} 3d$_{3/2}$ doublets is approximately 10:1, which suggests that the

10.1002/chem.202004217

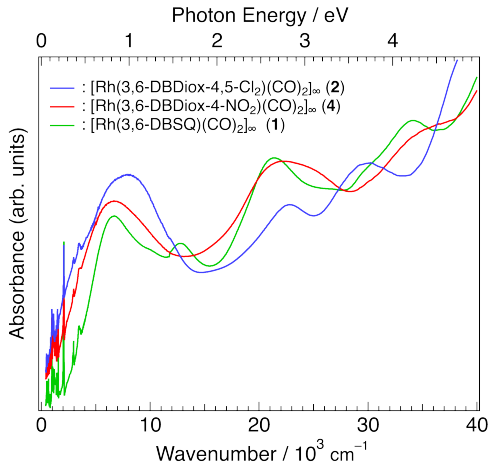

Figure 5. Vis–NIR–mid-IR spectrum of [Rh(3,6-DBDiox-4-NO_2)$(CO)_2]_\infty$ (**4**) in the solid-state (KBr pressed disk), together with those of [Rh^{I}(3,6-DBSQ)$(CO)_2]_\infty$ (**1**) and [$Rh^{I,II}$(3,6-DBDiox-4,5-Cl_2)$(CO)_2]_\infty$ (**2**). The Vis–NIR and mid-IR spectra were connected smoothly at approximately 4000–5000 cm^{-1}.

formal oxidation state of rhodium ions at RT is approximately $Rh^{1.09+}$ and the ratio of [Rh^{I}(3,6-DBSQ-4-NO_2)$(CO)_2$] to [Rh^{II}(3,6-DBCat-4-NO_2)$(CO)_2$] is approximately 10:1, where 3,6-DBSQ-4-NO_2 and 3,6-DBCat-4-NO_2 indicate 3,6-di-*tert*-butyl-4-nitro-1,2-benzosemiquinonato and 3,6-di-*tert*-butyl-4-nitrocatecholato, respectively.

Electronic absorption spectra

To better understand the electronic structure, the visible-near-infrared-mid-infrared (Vis–NIR–mid-IR) spectrum of **4** was measured, together with the spectra of **1** and **2** (Figure 5). Each compound exhibits intense absorption expanding from the NIR to mid-IR region, which is the absorption that appears by adopting a 1D chain structure. The absorption band for **1** with the maximum at 6700 cm^{-1} is assigned to the charge-transfer absorption from a filled 1D d-band to the vacant semiquinonato π* levels.[10d] The absorption band for **2** with the maximum at 8000 cm^{-1} extends widely from the NIR to mid-IR region compared with that of **1** and is considered to consist of several overlapping bands, including the intervalence charge-transfer transitions of $Rh^{2+} \leftarrow Rh^{+}$ and π*($SQ^{\bullet-}$) ← π*(Cat^{2-}) transition, in addition to the π*($SQ^{\bullet-}$) ← 1D d-band (d_z^2) transition.[9a] This broad band extends further from the mid-IR to the far-IR region, indicating the presence of low-energy electronic excitation in the Rh chain associated with $–Rh^{+}–Rh^{2+}– \leftarrow –Rh^{2+}–Rh^{+}–$.[18] In fact, **2** exhibits a high electrical conductivity of 17–34 S cm^{-1}.[9a] The absorption band for **4** with the maximum at 6700 cm^{-1} is clearly broader than that of **1** and extends to the far-IR region, as in the case of the band observed for **2**, although the degree of expansion of the band is small. Therefore, the origin of this absorption is considered to be the same as those of **2**, but the reason for the less broad feature is that the ratio of Rh(II)–catecholato to Rh(I)–semiquinonato in **4** is small. The broadening of the band reaching the far-IR region suggests that compound **4** will exhibit a relatively high conductivity.

Electrical properties

The temperature dependence of the electrical resistivity of **4** was measured along the chain axis *a* using a DC four-probe technique (Figure 6). The electrical conductivity at RT is a relatively high value of 2.9 × 10^{-2} S cm^{-1}. The resistivity does not depend much

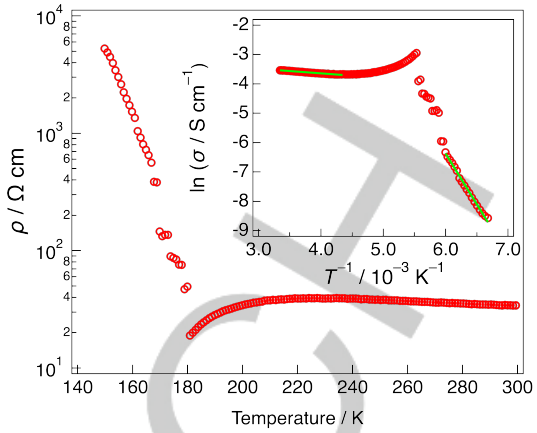

Figure 6. Temperature dependence of the electrical resistivity ρ and electrical conductivity σ of [Rh(3,6-DBDiox-4-NO_2)$(CO)_2]_\infty$ (**4**) measured along the chain axis *a*. The green solid lines indicate the fits to the data using the Arrhenius equation.

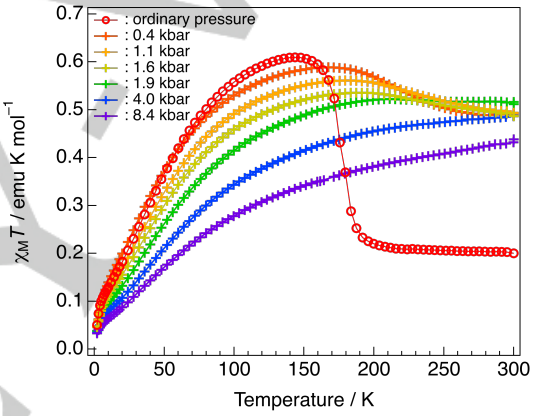

Figure 7. Temperature dependence of the molar magnetic susceptibility in the form of $\chi_M T$ vs. T plots for [Rh(3,6-DBDiox-4-NO_2)$(CO)_2]_\infty$ (**4**) measured on a polycrystalline sample under ordinary pressure and several static pressures up to 8.4 kbar. Each measurement was performed during a cooling process.

on the temperature down to 220 K and surprisingly decreases to the vicinity of the phase transition temperature and then increases rapidly in the LT phase. The observed decrease in the resistivity and the almost temperature-independent resistivity may indicate that **4** in the RT phase is in a metallic state. However, the electrical conductivity at RT is about two orders of magnitude smaller than the metallic 1D d-electronic metal complex conductors.[18a,19] This may be due to the fact that the carrier concentration is quite low due to the very small degree of partial oxidation and the electrons flowing in the 1D Rh chain are strongly affected by the large-amplitude vibrations of Rh atoms. Further studies will still be required to reveal whether the RT phase is in a metallic state or not. Another important feature of the electrical property of **4** is the crossover from a relatively high conducting state with a small activation energy of E_a = 13.1 meV (299–230 K) in the RT phase to a semiconductor with a large activation energy of E_a = 295 meV (167–150 K) in the LT phase. The observed relatively high electrical conductivity (~10^{-2} S cm^{-1}) and a small activation energy (13.1 meV) can be attributed to the Rh(I,II) mixed-valence state, in agreement with the XPS results. On the other hand, considering the typical semiconducting behavior with a large

10.1002/chem.202004217

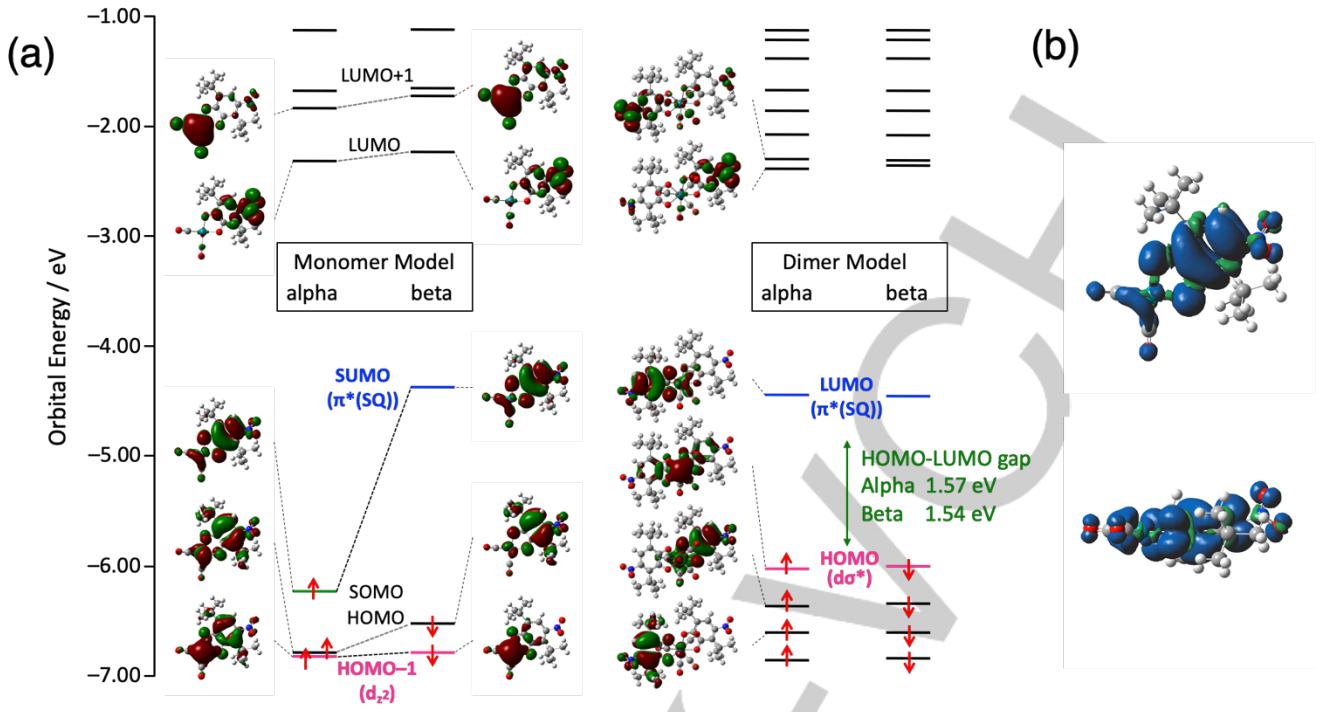

Figure 8. a) Frontier molecular orbitals and energies (eV) for the monomer and dimer models derived from the UB3LYP level calculation based on the structure determined at 129K. The MIDI + polarization function, 6-31G*, and 6-31+G* basis functions were used for Rh atom, 3,6-DBSQ-4-NO_2 ligand, and CO ligands, respectively. b) Spin-density isosurface (threshold = 0.004) of the monomer model at 129 K derived from the UB3LYP calculation. Blue and green lobes represent positive and negative spin densities, respectively.

activation energy in the LT phase, although complex molecules are stacked with equal spacing, it is natural to consider that the LT phase is a Rh(I)–semiquinonato state rather than a mixed-valence state. This result is the first example succeeded in band-filling control by using valence tautomerism.

Magnetic properties

The temperature dependence of the molar magnetic susceptibility of **4** was examined under ordinary pressure and several static pressures up to 8.4 kbar (Figure 7). Compound **4** exhibits a dramatic change in magnetic behavior with the phase transition. The $\chi_M T$ value at 300 K under ordinary pressure is 0.200 emu K mol^{-1}, which is 53 % of the spin-only value of S = 1/2 (0.375 emu K mol^{-1}). The $\chi_M T$ value increases very slightly with decreasing temperature in the RT phase and then increases rapidly with the phase transition up to the maximum of 0.603 emu K mol^{-1} at 140 K, before rapidly decreasing down to 0.050 emu K mol^{-1} at 2 K. The observed magnetic behavior is similar to that observed for compound **3** but does not exhibit a striking increase in $\chi_M T$ value, as observed in the LT phase of **3**.[10d]

Although compound **4** is an equally spaced molecule, the magnetic data in the RT phase show a significantly different behavior from the S = 1/2 1D Heisenberg antiferromagnetic chain model (Figure S7 in Supporting Information). For this reason, it is first considered that a little less than 10 % of this compound has been changed to the Rh(II)–catecholato complex, as suggested by the XPS spectrum. Second, although the $\chi_M T$ value at the RT is 53 % of the spin-only value, the $\chi_M T$ value slightly increases with decreasing temperature, suggesting that ferromagnetic interactions coexist in addition to the strong antiferromagnetic interactions. In the DFT calculations performed for the trimer model for compound **3**, we have already reported that the next-neighbor magnetic interaction is very large at J/k_B = –200.1 K.[10d] This magnetic interaction is expected to have a strong effect even in **4**. Therefore, the details of the magnetic interactions in **4** could not be well discussed. It is, however, apparent that not only the conductivity but also the magnetism varies dramatically due to the change in the electronic state accompanying the phase transition.

As shown in Figure 7, when pressure is applied, the transition point disappears, which is probably because the transition temperature shifts to a higher temperature by applying pressure. A similar shift of the transition point to RT with applying pressure has also been found in compound **3**, in which the transition point shifts to RT at a pressure of 1.6 kbar.[10d] As the applied pressure is increased, the swelling of the $\chi_M T$ value near 170 K decreases, and then the $\chi_M T$ value monotonically decreases with decreasing temperature under pressures above 1.9 kbar. The disappearance of the transition point with applied pressure is also confirmed by the temperature dependence of the electrical conductivity under pressure (Figure S8 in Supporting Information), and it is considered that the LT phase shifts to room temperature by applying the pressure. This behavior is because the LT phase with a short Rh–Rh distance is stabilized under pressure.

Density functional theory (DFT) calculations

To obtain information regarding the electronic structure and magnetic interaction for **4**, we performed DFT calculations based on the monomer and dimer models constructed from the atomic coordinates of the RT and LT phases. Selected frontier orbitals and their energies are shown in Figure 8a and Figure S9 in Supporting Information. Here, the SOMO, SUMO, HOMO, and LUMO denote the singly occupied, singly unoccupied, highest-occupied, and lowest-unoccupied molecular orbitals, respectively, and the molecular orbitals were obtained as the α and β orbitals

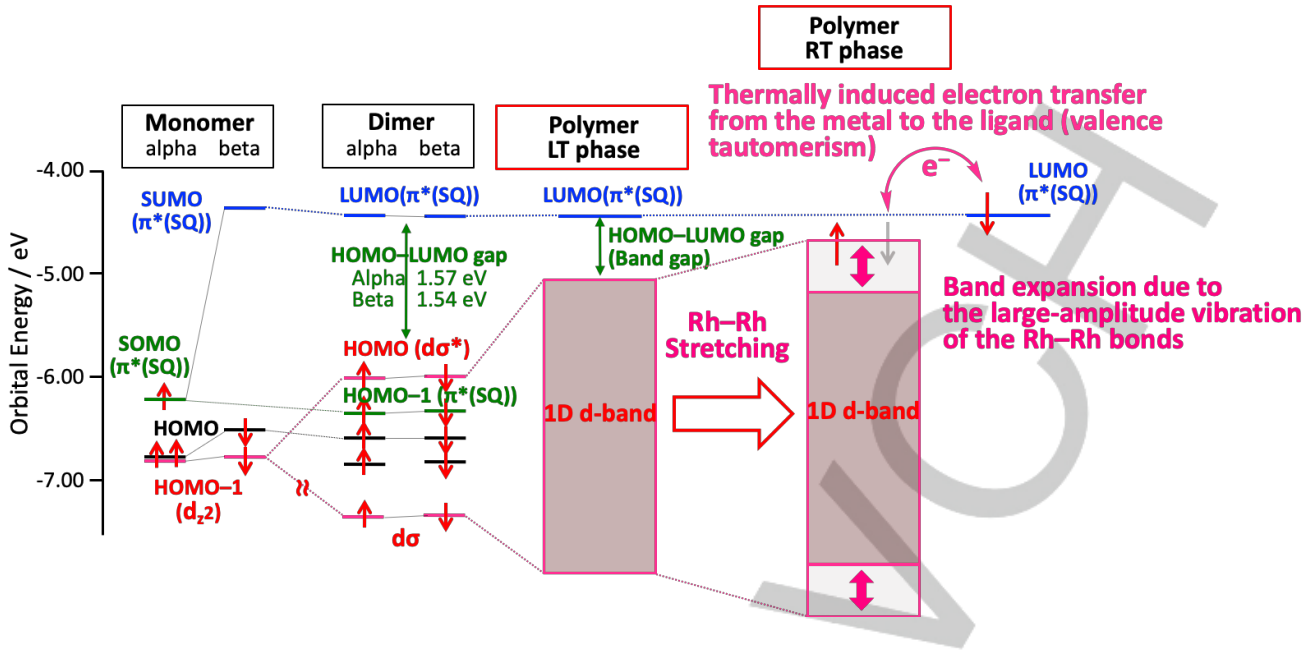

Figure 9. Band structure model predicted from the energy levels of the monomer and dimer models, and changes in energy levels accompanying the large-amplitude vibrations of rhodium atoms.

due to the spin-unrestricted formalism. The spin densities of the monomer models based on the structures at 129 K and 228 K are shown in Figure 8b and Figure S10 in Supporting Information, respectively. In either case, the spin density is delocalized to the whole molecule, except for the *t*-butyl groups, but is not very present on the rhodium atom. Since no obvious difference in the electronic state due to the difference in the temperatures at 129 K and 228 K was confirmed, the results for the 129 K data will be described.

The *α*-SOMO and *β*-SUMO of the monomer model are predominantly the semiquinonato π* orbitals with some contributions from the Rh dπ orbital and carbonyl ligands. The HOMOs primarily comprise a semiquinonato π* orbital with some contribution from a Rh dπ orbital. The d_{z^2} orbital that consists of the 1D d-band greatly contributes to the HOMO–1s. On the other hand, unlike the monomer model, the HOMO of the dimer model is composed of the HOMO–1s of the monomer model derived from the d_{z^2} orbitals, and the SOMO–HOMO energy level conversion has occurred. This conversion is due to a large orbital splitting of dσ and dσ* orbitals caused by the large overlap of d_{z^2} orbitals between monomers. Moreover, the LUMO of the dimer model originating from the SUMO of the monomer exists at approximately –4.4 eV, and its energy level is almost the same as the SUMO level of the monomer because there is no direct overlap between semiquinonato ligands.

To estimate the effective exchange integral J_{ab}, we calculated the energies of the high-spin (HS) triplet state and the low-spin (LS) spin-singlet state of the dimer units at 228 K and 129 K (Table S2 in Supporting Information).[20] The effective exchange integrals J_{ab}/k_B at 228 K and 129 K estimated from these energy values based on the following equation were –433 K and –462 K, respectively, which suggests that both intrachain magnetic interactions are strongly antiferromagnetic:

$$H = -\sum_{a,b} J_{ab}\, S_a \cdot S_b$$

$$J_{ab} = \frac{E^{LS} - E^{HS}}{2(\langle S^2\rangle^{HS} - \langle S^2\rangle^{LS})}$$

where E^X and $\langle S^2\rangle^X$ represent the total energies and the $\langle S^2\rangle$ values of the spin state X (X = HS or LS), respectively. Therefore, the difference in the magnetic behavior between the LT and RT phases could not be deduced by the DFT calculation based on the dimer models.

Dynamic mixed-valence state

Although the DFT calculations have only been performed up to the dimer model, it is expected that the splitting between the dσ and dσ* orbitals becomes large with an increasing number of interacting complex molecules. The band structure model predicted from the DFT calculations based on the monomer and dimer models is shown in Figure 9. In the polymeric structure, the further overlap of d_{z^2} orbitals is expected to form much wider 1D d-bands and reduce the HOMO–LUMO gap since the LUMO comprised of a semiquinonato π* orbital exists at almost the same level as the SUMO of the monomer. Judging from the typical semiconducting behavior, the LT phase is considered to be a Rh(I)–semiquinonato complex, and therefore, the upper part of the filled d-band is expected to be relatively far from the empty π* level of the semiquinonato ligand. As already described, there was no significant difference in the HOMO–LUMO gap estimated for the dimer models at 129 K and 228 K. However, the obvious structural difference between the LT and RT phases is the large-amplitude vibration of the rhodium atoms and its surrounding coordinated atoms in the 1D chain direction, which is only observed in the RT phase. Since the influence of the molecular vibration is not included in the DFT calculations, it is considered that no difference between the two phases was observed.

The thermal vibration of rhodium atoms contains the contribution of lattice vibration (including the libration and vibration of the whole molecule), in addition to the large-amplitude

vibration of the rhodium atoms along the 1D chain. As a very rough approximation, assuming that the mean square displacement values in another two directions perpendicular to the 1D chain (U_{22} = 0.02948 (14), U_{33} = 0.03073 (13) Å^2) are the contributions from lattice vibration, its magnitude is estimated from the average of these values. Subtracting this averaged value from the mean square displacement in the 1D chain direction (U_{11} = 0.0676 (4) Å^2) and calculating the square root of it, the deviation in the 1D chain direction from the equilibrium position of the rhodium atom is estimated to be 0.19 Å. As already mentioned above, this large-amplitude vibration of the Rh–Rh bonds is tentatively inferred to be a phonon mode like the phonon mode 2 (Figure S6c in Supporting Information), due to the existence of the two-fold periodicity of the –Rh–Rh– period. Considering the effect of the large-amplitude vibration of rhodium atoms on the thermally induced metal–ligand electron transfer (valence tautomerism) and vice versa, we propose a band structure model shown in Figure 9. When the Rh–Rh distance is largely reduced due to the increase in the amplitude of the Rh–Rh stretching vibration by thermal excitation, the 1D d-band expands, and the upper part of the band is very close to the vacant semiquinonato π* level. This situation will allow the thermally induced electron transfer from the rhodium(I) ion to the semiquinonato ligand, resulting in the Rh(I,II)–semiquinonato/catecholato mixed–valence state, which further causes a decrease in the Rh–Rh distances by removing the electrons from the antibonding orbitals of the 1D d-band. Thus, it is considered that the coupling of the thermally induced metal–ligand electron transfer (valence tautomerism) with the large-amplitude vibration of the Rh–Rh bonds causes a dynamic mixed-valence state, producing approximately 10 % of [Rh^{II}(3,6-DBCat-4-NO$_2$)(CO)$_2$]. Finally, as described above, the present phase transition exhibited a comparatively larger transition entropy than that for the typical displacive type phase transition.[17] Such a large entropy change would arise from the softening of the vibrational modes due to the phase transition, which is consistent with the above situation.

Conclusions

As mentioned in the introduction, since VT complexes have two nearly degenerate electronic states, the interconversion of electrical, magnetic, or optical properties using the switching of valence tautomerism by external stimuli has been vigorously studied. However, there is currently no example of a dynamic mixed-valence state originating from the combination of valence tautomerism with large-amplitude molecular vibrations. The present compound **4** is the first example of the dynamic mixed-valence state originating from the metal–ligand electron transfer (valence tautomerism) coupled with the large-amplitude vibration of the metal–metal bonds. We have also reported a 1D iodido-bridged mixed-valence diplatinum(II,III) complex [Pt$_2$(EtCS$_2$)$_4$I]$_\infty$ that exhibits a metallic state above 204 K originating from the electron transfer between diplatinum units coupled with the large-amplitude vibration of the bridging iodido ions.[19] Electron transfer coupled with molecular vibrations is very important since it may create new research fields in the chemistry and physics of dynamic molecular crystals based on dynamic electronic states arising from the mixing of different electronic states by nuclear displacements. We will continue to search for molecular materials that exhibit unique physical properties originating from the dynamic mixed-valence state that appears by the coupling of electron transfer with molecular vibrations.

Experimental Section

General

All syntheses were performed under an argon atmosphere using standard vacuum-line and Schlenk techniques. All solvents were dried using appropriate drying agents and were freshly distilled under argon before use.[21] ^{1}H and ^{13}C NMR spectra were obtained on a JEOL ECA-600 spectrometer using tetramethylsilane (TMS) as an internal standard. Elemental analyses were performed at the Center for Organic Elemental Microanalysis of the Graduate School of Pharmaceutical Sciences, Kyoto University.

Syntheses

Dodecacarbonyltetrarhodium(0) ([Rh$_4$(CO)$_{12}$])[22], [Rh(3,6-DBSQ)(CO)$_2$]$_\infty$ (**1**)[10d], and [Rh(3,6-DBDiox-4,5-Cl$_2$)(CO)$_2$]$_\infty$ (**2**)[9a] were prepared according to published procedures. The synthesis of 3,6-di-*tert*-butyl-4-nitro-1,2-benzoquinone (3,6-DBBQ-4-NO$_2$) was performed after improving the literature method and once isolating the intermediate of 3,6-di-*tert*-butyl-5,6-dinitro-3-cyclohexene-1,2-dione.[23]

Synthesis of 3,6-di-*tert*-butyl-5,6-dinitro-3-cyclohexene-1,2-dione: To a solution of 3,6-di-*tert*-butylcatechol (2.202 g, 9.904 mmol) dissolved in 25 mL of acetic acid, a mixture of 2.00 mL (43.8 mmol) of nitic acid (S.G.=1.38) and 5 mL of acetic acid was slowly added dropwise, with stirring in an oil bath, at room temperature. The resulting black solution was heated at 50 °C for 7 h to produce a bright yellowish orange suspension. After cooling to room temperature, the suspension was cooled overnight at 0 °C. The precipitate was filtered through a glass filter. The collected solid was rinsed with ice-cooled hexane and dried in vacuo to afford a bright yellow powder (902 mg, 29%). ^{1}H NMR (600 MHz, CDCl$_3$): δ=1.15 (s, 9H, *t*-butyl), 1.25 (s, 9H, *t*-butyl), 6.29 (d, J = 7.6 Hz, 1H, –CH(NO$_2$)–C<u>H</u>=), 7.17 (d, J = 7.6 Hz, 1H, –C<u>H</u>(NO$_2$)–CH=).

Synthesis of 3,6-di-*tert*-butyl-4-nitro-1,2-benzoquinone (3,6-DBBQ-4-NO$_2$): To a solution of 3,6-di-*tert*-butyl-5,6-dinitro-3-cyclohexene-1,2-dione (1.706 g, 5.462 mmol) in 45 mL of dichloromethane, a solution of diethylamine (0.7 mL, 6.77 mmol) in 10 mL of dichloromethane was slowly added dropwise, with stirring, at room temperature. The color of the reaction mixture changed from bright yellow to black. After 1 h, the black reaction mixture was washed with 5 % NaCl solution (100 mL × 3) until the washings became neutral, and then the aqueous phase was extracted with dichloromethane (100 mL × 2). The combined organic phases were dried over anhydrous Na$_2$SO$_4$. After filtration, the solution was concentrated until dryness using a rotatory evaporator. The resulting residue was purified by silica gel column chromatography using hexane–diethyl ether (10:1, v/v) as the eluent to render 3,6-DBBQ-4-NO$_2$ as a dark green powder. The crude product was recrystallized twice by dissolving it in a minimal amount of diethyl ether, adding hexane with a forming layer, and then cooling the solution overnight in a freezer at –60 °C to produce pure 3,6-DBBQ-4-NO$_2$ as a dark green powder (815 mg, 72%). ^{1}H NMR (600 MHz, CDCl$_3$): δ=1.27 (s, 9H, *t*-butyl), 1.38 (s, 9H, *t*-butyl), 6.39 (s, 1H, –C(NO$_2$)=CH–); ^{13}C NMR (600 MHz, CDCl$_3$): δ=28.7 (CH$_3$), 28.8 (CH$_3$), 35.6 (CMe$_3$), 36.5 (CMe$_3$), 131.2 (C(5)H), 139.3 (ring C(3)), 151.8 (ring C(6)), 153.1 (C(4)NO$_2$), 178.8 (C(1)=O), 182.5 (C(2)=O); elemental analysis calcd for C$_{14}$H$_{19}$NO$_4$: C 63.38, H 7.22, N 5.28, found: C 63.22, H 7.21, N 5.29.

Synthesis of [Rh(3,6-DBDiox-4-NO$_2$)(CO)$_2$]$_\infty$ (4): Bubnov et al. reported the synthesis of compound **4** by the reaction of Tl(3,6-DBSQ-4-NO$_2$) with [RhCl(CO)$_2$]$_2$ in toluene.[24] We prepared compound **4** using our developed redox reaction of [Rh$_4$(CO)$_{12}$] with the corresponding benzoquinone derivative. [Rh$_4$(CO)$_{12}$] (37.35 mg, 50.0 μmol) and 3,6-DBBQ-4-NO$_2$ (53.35 mg, 201 μmol) were placed in a small cut vial (10 mm i.d., 30 mm height) and a large sealable vial (15.0 mm i.d., 50 mm height), respectively. The small vial was placed inside the large sealable vial such that 3,6-DBBQ-4-

NO_2 was not buried under the small vial. After filling the large sealable vial with a mixture of hexane–toluene (3:1, v/v), well-shaped dark brown needle crystals of **4** grew within 2 weeks via the slow diffusion of $[Rh_4(CO)_{12}]$ and 3,6-DBBQ-4-NO_2. The resulting needle crystals of **4** were collected by suction filtration and were rinsed with ice-cooled hexane (57.58 mg, 68%). Elemental analysis calcd for $C_{16}H_{19}NO_6Rh$: C 45.30, H 4.51, N 3.30, found: C 45.15, H 4.50, N 3.31.

X-ray Photoelectron Spectroscopy (XPS)

XPS data were obtained on a VG Scientific ESCALAB 220i-XL spectrometer equipped with a non-monochromatized Mg Kα radiation source (1253.6 eV) operated at 15 kV and 20 mA. Measurements were conducted in the 10^{-6} Pa pressure range. Samples were ground into powders and spread onto the conductive adhesive tape attached to sample holders. The absence of X-ray beam effects was verified by the X-ray power dependence of the XPS spectra. The carbon 1s binding energy (284.6 eV) was used to calibrate the binding energies. Curve-fitting analysis was performed with the iterative least squares computer program XPSPEAK41 using a combination of Gaussian and Lorentzian line shapes.

Calorimetry

Heat capacity measurements were performed in the temperature range of 7–302 K with a laboratory-made LT adiabatic calorimeter for small samples.[25] A sample of 0.11413 g after the buoyancy correction was loaded into a gold-plated copper cell and sealed under helium gas at ambient pressure using an indium gasket. The helium gas functions as a heat-exchange medium. Thermometry was performed with a rhodium-iron alloy resistance thermometer (nominal 27 Ω, Oxford Instruments) calibrated on the basis of the international temperature scale of 1990 (ITS-90).

X-ray Crystal Structure Analyses

Single-crystal X-ray diffraction data were collected at 10 temperatures ranging from 288 K to 35 K on two different crystals. Crystals of **4** were mounted on glass fibers using Apiezon grease. X-ray diffraction experiments in-house were performed using Mo Kα radiation of λ = 0.71075 Å on a Rigaku Saturn 724 HG CCD detector with a MicroMax007 HF DW X-ray generator installed at Okayama University of Science. The temperature of the crystal was controlled by a Rigaku variable-temperature apparatus based on a cold nitrogen gas stream method. X-ray diffraction experiments using a synchrotron radiation source (λ = 0.68869 Å) were performed at the Photon Factory (PF) BL-8A in the High Energy Accelerator Research Organization (KEK), Japan. The diffraction data were collected on a Rigaku imaging-plate area detector system equipped with a cold helium gas flow-type system for the LT experiments. Data collection, cell refinements, indexing, peak integrations, and the scaling of the diffraction data were performed using CrystalClear software for the in-house data and RAPID AUTO software for the synchrotron radiation data. Lorentz, polarization, and multi-scan absorption corrections were applied to the intensity data.

The structures were solved by a direct method using the SHELXS program and refined by a full-matrix least squares method on F^2 for all reflections utilizing the SHELXL-2018/1 or -2018/3 program.[26] The X-ray analyses were performed using the free GUI software Yadokari-XG.[27] All non-hydrogen atoms were refined anisotropically, whereas hydrogen atoms on the methyl groups were placed in geometrically calculated positions using a riding model and were refined using the isotropic displacement parameters derived from their parent atoms. Further details of the crystal data and crystal structure refinements for **4** are available in the Supporting Information. Deposition Numbers CCDC-2027122–2027131 contain the supplementary crystallographic data for 206 K, 101 K, 156 K, 173 K, 288 K, 228 K, 129 K, 254 K, 153 K, and 35 K data, respectively. These data are provided free of charge by the joint Cambridge Crystallographic Data Centre and Fachinformationszentrum Karlsruhe Access Structures service www.ccdc.cam.ac.uk/structures.

UV–Visible–Near-IR and IR Spectroscopies

UV-visible-near-IR spectra of complexes **1**, **2** and **4** as KBr pressed disks were recorded on a Hitachi U-3500 spectrophotometer equipped with a 60-mm-i.d. integrating-sphere apparatus. IR spectra were recorded as KBr pressed disks on a JASCO FT/IR-4100 spectrophotometer.

Magnetic Measurements

Magnetic measurements were performed using a Quantum Design MPMS-5SH or MPMS-XL7 SQUID magnetometer. A polycrystalline sample (27.64 mg) of **4** held in a polyethylene film (19.97 mg) inside a plastic straw was used. Magnetic susceptibility measurements on the polycrystalline sample were performed from 350 K to 2 K under an applied magnetic field of 1 kOe. The diamagnetic contributions of the polyethylene film and plastic straw were measured from 350 to 2 K under an applied magnetic field of 10 kOe, and the corresponding diamagnetic contribution obtained by multiplying the measured value by a factor of 1000/10000 was subtracted from the raw data. The paramagnetic component of the molar magnetic susceptibility (χ_M) was obtained after subtraction of the calculated diamagnetic core contribution (-181.5×10^{-6} emu mol^{-1}) estimated from the measured diamagnetic susceptibility of 3,6-di-*tert*-butyl-4-nitro-1,2-benzoquinone (3,6-DBBQ-4-NO_2) (-121.5×10^{-6} emu mol^{-1}) and Pascal's constants for a rhodium(0) atom and two carbon monoxide ligands. Magnetic measurements under various static pressures up to 8.4 kbar were performed using a piston-cylinder-type pressure cell constructed from a Cu–Be alloy. The crystals (10.75 mg) were dispersed into a pressure-transmitting medium, Daphne 7373, with a piece of tin as the manometer in a Teflon bucket. The actual pressure was calibrated using the superconducting transition temperature of tin.

Electrical Resistivity Measurements

Direct current electrical resistivity measurements along the 1D chain direction were performed on several single crystals by the four-probe method. The electrical contacts between the sample and 15 μm o.d. gold wires were created using gold paint. The sample temperature was controlled using a closed-cycle helium refrigerator (Iwatani, CryoMini D105). The electrical resistivity under static pressure up to 12 kbar (1.2 GPa) was measured using a clamp-type pressure cell purchased from Kitano Seiki Co., Ltd.

Density functional theory (DFT) calculations

We performed DFT calculations based on the monomer and dimer models of **4** in the RT and LT phases constructed from the atomic coordinates at 228 K and 129 K, respectively. All calculations were performed using an unrestricted B3LYP (UB3LYP) method with basis sets of MIDI + polarization function, 6-31G*, and 6-31+G* for the Rh atoms, 3,6-DBSQ-4-NO_2 ligand, and CO ligands, respectively. All calculations were carried out using the Gaussian 09 program.[28]

Acknowledgements

This study was supported by JSPS KAKENHI Grant Number JP JP23110723 (Molecular Degree of Freedom), 17H05389 (Coordination Asymmetry). The synchrotron X-ray diffraction experiment was performed under the approval of the Photon Factory Program Advisory Committee (Proposal No. 2014G710). We also thank the Instrument Center at the Institute for Molecular Science, for the use of an X-ray photoelectron spectrometer (VG Scientific ESCALAB 220i-XL spectrometer) and a SQUID magnetometer (Quantum Design MPMS-XL7).

Conflict of interest

The authors declare no conflict of interest.

Keywords: conducting materials • mixed-valent compounds • valence tautomerism • vibronic interaction • large-amplitude vibration

[1] a) Z. S. Yao, Z. Tang, J. Tao, *Chem. Commun.* **2020**, *56*, 2071–2086; b) Y. S. Meng, T. Liu, *Acc. Chem. Res.* **2019**, *52*, 1369–1379; c) J. Ferrando-Soria, J. Vallejo, M. Castellano, J. Martinez-Lillo, E. Pardo, J. Cano, I. Castro, F. Lloret, R. Ruiz-Garcia, M. Julve, *Coord. Chem. Rev.* **2017**, *339*, 17–103; d) O. Sato, *Nat. Chem.* **2016**, *8*, 644–656; e) E. Coronado, G. Minguez Espallargas, *Chem. Soc. Rev.* **2013**, *42*, 1525–1539; f) V. I. Minkin, *Russ. Chem. Bull.* **2008**, *57*, 687–717; g) O. Sato, J. Tao, Y.-Z. Zhang, *Angew. Chem. Int. Ed.* **2007**, *46*, 2152–2187; h) A. Dei, D. Gatteschi, C. Sangregorio, L. Sorace, *Acc. Chem. Res.* **2004**, *37*, 827–835; i) O. Kahn, J. P. Launay, *Chemtronics* **1988**, *3*, 140–151.

[2] a) J. Chen, Y. Sekine, A. Okazawa, H. Sato, W. Kosaka, H. Miyasaka, *Chem. Sci.* **2020**, *11*, 3610–3618; b) J. Chen, Y. Sekine, Y. Komatsumaru, S. Hayami, H. Miyasaka, *Angew. Chem. Int. Ed.* **2018**, *57*, 12043–12047; c) J. A. DeGayner, K. Wang, T. D. Harris, *J. Am. Chem. Soc.* **2018**, *140*, 6550–6553; d) J. Guasch, L. Grisanti, S. Jung, D. Morales, G. D'Avino, M. Souto, X. Fontrodona, A. Painelli, F. Renz, I. Ratera, J. Veciana, *Chem. Mater.* **2013**, *25*, 808−814; e) H. Miyasaka, N. Motokawa, T. Chiyo, M. Takemura, M. Yamashita, H. Sagayama, T. H. Arima, *J. Am. Chem. Soc.* **2011**, *133*, 5338–5345; f) T. Mahfoud, G. Molnar, S. Bonhommeau, S. Cobo, L. Salmon, P. Demont, H. Tokoro, S. I. Ohkoshi, K. Boukheddaden, A. Bousseksou, *J. Am. Chem. Soc.* **2009**, *131*, 15049–15054; g) S. Horiuchi, Y. Okimoto, R. Kumai, Y. Tokura, *Science* **2003**, *299*, 229–232; h) N. Kojima, W. Aoki, M. Itoi, Y. Ono, M. Seto, Y. Kobayashi, Y. Maeda, *Solid State Commun.* **2001**, *120*, 165–170; i) J. B. Torrance, J. E. Vazquez, J. J. Mayerle, V. Y. Lee, *Phys. Rev. Lett.* **1981**, *46*, 253–257.

[3] a) A. Diaconu, S. L. Lupu, I. Rusu, I. M. Risca, L. Salmon, G. Molnar, A. Bousseksou, P. Demont, A. Rotaru, *J. Phys. Chem. Lett.* **2017**, *8*, 3147–3151; b) K. Bairagi, O. Iasco, A. Bellec, A. Kartsev, D. Li, J. Lagoute, C. Chacon, Y. Girard, S. Rousset, F. Miserque, Y. J. Dappe, A. Smogunov, C. Barreteau, M. L. Boillot, T. Mallah, V. Repain, *Nat. Commun.* **2016**, 7:12212; c) T. Matsumoto, G. N. Newton, T. Shiga, S. Hayami, Y. Matsui, H. Okamoto, R. Kumai, Y. Murakami, H. Oshio, *Nat. Commun.* **2014**, 5:3865; d) *Spin-Crossover Materials: Properties and Applications*, M. A. Halcrow ed., John Wiley & Sons, Ltd., **2013**; e) M. Clemente-León, E. Coronado, M. López-Jordà, J. C. Waerenborgh, C. Desplanches, H. Wang, J.-F. Létard, A. Hauser, A. Tissot, *J. Am. Chem. Soc.* **2013**, *135*, 8655−8667; f) A. Bousseksou, G. Molnar, L. Salmon, W. Nicolazzi, *Chem. Soc. Rev.* **2011**, *40*, 3313–3335; g) P. Gütlich, A. B. Gaspar, Y. Garcia, V. Ksenofontov, *C. R. Chimie* **2007**, *10*, 21–36; h) A. Hauser, in *Topics in Current Chemistry, Vol. 234* (Eds.: P. Gütlich, H. A. Goodwin), Springer-Verlag, **2004**, pp. 155–198; i) O. Kahn, C. J. Martinez, *Science* **1998**, *279*, 44–48.

[4] a) M. Nihei, Y. Yanai, I. J. Hsu, Y. Sekine, H. Oshio, *Angew. Chem. Int. Ed.* **2017**, *129*, 606–609; b) N. Hoshino, F. Iijima, G. N. Newton, N. Yoshida, T. Shiga, H. Nojiri, A. Nakao, R. Kumai, Y. Murakami, H. Oshio, *Nat. Chem.* **2012**, *4*, 921–926; c) C. P. Berlinguette, A. Dragulescu-Andrasi, A. Sieber, H.-U. Güdel, C. Achim, K. R. Dunbar, *J. Am. Chem. Soc.* **2005**, *127*, 6766–6779; d) M. E. Itkis, X. Chi, A. W. Cordes, R. C. Haddon, *Science* **2002**, *296*, 1443–1445.

[5] a) M. Mitsumi, K. Ezaki, Y. Komatsu, K. Toriumi, T. Miyatou, M. Mizuno, N. Azuma, Y. Miyazaki, M. Nakano, Y. Kitagawa, T. Hanashima, R. Kiyanagi, T. Ohhara, K. Nakasuji, *Chem. Eur. J.* **2015**, *21*, 9682–9696; b) S. Horiuchi, Y. Tokunaga, G. Giovannetti, S. Picozzi, H. Itoh, R. Shimano, R. Kumai, Y. Tokura, *Nature* **2010**, *463*, 789–792.

[6] a) M. Tadokoro, H. Hosoda, T. Inoue, A. Murayama, K. Noguchi, A. Iioka, R. Nishimura, M. Itoh, T. Sugaya, H. Kamebuchi, M. A. Haga, *Inorg. Chem.* **2017**, *56*, 8513–8526; b) A. Ueda, S. Yamada, T. Isono, H. Kamo, A. Nakao, R. Kumai, H. Nakao, Y. Murakami, K. Yamamoto, Y. Nishio, H. Mori, *J. Am. Chem. Soc.* **2014**, *136*, 12184–12192; c) K. Nakasuji, K. Sugiura, T. Kitagawa, J. Toyoda, H. Okamoto, K. Okaniwa, T. Mitani, H. Yamamoto, I. Murata, A. Kawamoto, J. Tanaka, *J. Am. Chem. Soc.* **1993**, *113*, 1862–1864.

[7] a) D. Z. S. Yao, S. Q. Wu, Y. Kitagawa, S. Q. Su, Y. G. Huang, G. L. Li, Z. H. Ni, H. Nojiri, Y. Shiota, K. Yoshizawa, S. Kang, S. Kanegawa, O. Sato, *Angew. Chem. Int. Ed.* **2017**, *56*, 717–721; b) J. Harada, M. Ohtani, Y. Takahashi, T. Inabe, *J. Am. Chem. Soc.* **2015**, *137*, 4477–4486.

[8] a) T. Tezgerevska, K. G. Alley, C. Boskovic, *Coord. Chem. Rev.* **2014**, *268*, 23–40; b) E. Evangelio, D. Ruiz-Molina, *C. R. Chimie* **2008**, *11*, 1137–1154; c) E. Evangelio, D. Ruiz-Molina, *Eur. J. Inorg. Chem.* **2005**, 2957–2971; d) D. N. Hendrickson, C. G. Pierpont, in *Topics in Current Chemistry, Vol. 234* (Ed.: H. A. G. Philipp Gütlich), Springer-Verlag **2004**, pp. 63–95; e) C. G. Pierpont, *Coord. Chem. Rev.* **2001**, *216–217*, 99–125; f) P. Gütlich, A. Dei, *Angew. Chem. Int. Ed. Engl.* **1997**, *36*, 2734–2736; g) C. G. Pierpont, C. W. Lange, *Prog. Inorg. Chem.* **1994**, *41*, 331–442; h) G. A. Abakumov, V. K. Cherkasov, M. P. Bubnov, O. G. Ellert, Z. V. Dobrokhotova, L. N. Zakharov, Y. T. Struchkov, *Dokl. Akad. Nauk SSSR* **1993**, *328*, 332–335; i) G. A. Abakumov, V. K. Cherkasov, A. V. Lobanov, *Dokl. Akad. Nauk SSSR* **1982**, *266*, 361–363; j) R. M. Buchanan, C. G. Pierpont, *J. Am. Chem. Soc.* **1980**, *102*, 4951–4957.

[9] a) M. Mitsumi, H. Goto, S. Umebayashi, Y. Ozawa, M. Kobayashi, T. Yokoyama, H. Tanaka, S.-i. Kuroda, K. Toriumi, *Angew. Chem. Int. Ed.* **2005**, *44*, 4164−4168; b) O.-S. Jung, C. G. Pierpont, *J. Am. Chem. Soc.* **1994**, *116*, 2229–2230.

[10] a) G. K. Gransbury, B. N. Livesay, J. T. Janetzki, M. A. Hay, R. W. Gable, M. P. Shores, A. Starikova, C. Boskovic, *J. Am. Chem. Soc.* **2020**, *142*, 10692–10704; b) B. Li, Y. M. Zhao, A. Kirchon, J. D. Pang, X. Y. Yang, G. L. Zhuang, H. C. Zhou, *J. Am. Chem. Soc.* **2019**, *141*, 6822–6826; c) S. Kanegawa, Y. Shiota, S. Kang, K. Takahashi, H. Okajima, A. Sakamoto, T. Iwata, H. Kandori, K. Yoshizawa, O. Sato, *J. Am. Chem. Soc.* **2016**, *138*, 14170–14173; d) M. Mitsumi, T. Nishitani, S. Yamasaki, N. Shimada, Y. Komatsu, K. Toriumi, Y. Kitagawa, M. Okumura, Y. Miyazaki, N. Górska, A. Inaba, A. Kanda, N. Hanasaki, *J. Am. Chem. Soc.* **2014**, *136*, 7026–7037; e) C. Carbonera, A. Dei, J. F. Létard, C. Sangregorio, L. Sorace, *Angew. Chem. Int. Ed.* **2004**, *43*, 3136–3138; f) D. M. Adams, B. Li, J. D. Simon, D. N. Hendrickson, *Angew. Chem. Int. Ed.* **1995**, *34*, 1481–1483; g) David M. Adams, Andrea Dei, Arnold L. Rheingold, D. N. Hendrickson, *J. Am. Chem. Soc.* **1993**, *115*, 8221–8229.

[11] A. Lannes, Y. Suffren, J. B. Tommasino, R. Chiriac, F. Toche, L. Khrouz, F. Molton, C. Duboc, I. Kieffer, J. L. Hazemann, C. Reber, A. Hauser, D. Luneau, *J. Am. Chem. Soc.* **2016**, *138*, 16493–16501.

[12] S. Q. Wu, M. Liu, K. Gao, S. Kanegawa, Y. Horie, G. Aoyama, H. Okajima, A. Sakamoto, M. L. Baker, M. S. Huzan, P. Bencok, T. Abe, Y. Shiota, K. Yoshizawa, W. Xu, H. Z. Kou, O. Sato, *Nat. Commun.* **2020**, 11:1992.

[13] T. M. Francisco, W. J. Gee, H. J. Shepherd, M. R. Warren, D. A. Shultz, P. R. Raithby, C. B. Pinheiro, *J. Phys. Chem. Lett.* **2017**, *8*, 4774–4778.

[14] O. Reu, S. Ostrovsky, S. Decurtins, S. X. Liu, S. Klokishner, *Eur. J. Inorg. Chem.* **2017**, 5356–5365.

[15] I. N. Markevtsev, M. P. Monakhov, V. V. Platonov, A. S. Mischenko, A. K. Zvezdin, M. P. Bubnov, G. A. Abakumov, V. K. Cherkasov, *J. Magn. Magn. Mater.* **2006**, *300*, e407–e410.

[16] a) C. W. Lange, M. Földeàki, V. I. Nevodchikov, V. K. Cherkasov, G. A. Abakumov, C. G. Pierpont, *J. Am. Chem. Soc.* **1992**, *114*, 4220–4222; b) V. I. Nevodchikov, G. A. Abakumov, V. K. Cherkasov, G. A. Razuvaev, *J. Organomet. Chem.* **1981**, *214*, 119–124.

[17] K. Nomoto, T. Atake, B. K. Chaudhuri, H. Chihara, *J. Phys. Soc. Jpn.* **1983**, *52*, 3475–3485.

[18] a) M. Mitsumi, H. Ueda, K. Furukawa, Y. Ozawa, K. Toriumi, M. Kurmoo, *J. Am. Chem. Soc.* **2008**, *130*, 14102–14104; b) J. B. Torrance, B. A. Scott, B. Welber, F. B. Kaufman, P. E. Seiden, *Phys. Rev. B* **1979**, *19*, 730–741.

[19] M. Mitsumi, T. Murase, H. Kishida, T. Yoshinari, Y. Ozawa, K. Toriumi, T. Sonoyama, H. Kitagawa, T. Mitani, *J. Am. Chem. Soc.* **2001**, *123*, 11179–11192.

[20] T. Soda, Y. Kitagawa, T. Onishi, Y. Takano, Y. Shigeta, H. Nagao, Y. Yoshioka, K. Yamaguchi, *Chem. Phys. Lett.* **2000**, *319*, 223–230.

[21] D. D. Perrin, W. L. F. Armarego, *Purification of laboratory chemicals*, Pergamon Press, New York, **1988**.

[22] S. Martinengo, G. Gxordano, P. Chini, G. W. Parshall, E. R. Wonchoba, *Inorg. Synth.* **1990**, *28*, 242–245.

[23] S. A. Chesnokov, V. K. Cherkasov, Y. V. Chechet, N. I. Nevodchikov, G. A. Abakumov, O. N. Mamysheva, *Russ. Chem. Bull.* **2000**, *49*, 1506–1511.

[24] M. P. Bubnov, I. A. Teplova, K. A. Kozhanov, G. A. Abakumov, V. K. Cherkasov, *J. Magn. Reson.* **2011**, *209*, 149–155.

[25] Y. Kume, Y. Miyazaki, T. Matsuo, H. Suga, *J.Phys. Chem. Solids* **1992**, *53*, 1297–1304.

[26] a) G. M. Sheldrick, *Acta Cryst.* **2008**, *A64*, 112–122; b) G. M. Sheldrick, *Acta Crystallogr., Sect. C* **2015**, *71*, 3–8.

[27] a) C. Kabuto, S. Akine, T. Nemoto, E. Kwon, *J. Cryst. Soc. Jpn.* **2009**, *51*, 218–224; b) K. Wakita, **2001**.

[28] M. J. Frisch, G. W. Trucks, H. B. Schlegel, G. E. Scuseria, M. A. Robb, J. R. Cheeseman, G. Scalmani, V. Barone, B. Mennucci, G. A. Petersson, H. Nakatsuji, M. Caricato, X. Li, H. P. Hratchian, A. F. Izmaylov, J. Bloino, G. Zheng, J. L. Sonnenberg, M. Hada, M. Ehara, K. Toyota, R. Fukuda, J. Hasegawa, M. Ishida, T. Nakajima, Y. Honda, O. Kitao, H. Nakai, T. Vreven, J. Montgomery, J. A., J. E. Peralta, F. Ogliaro, M. Bearpark, J. J. Heyd, E. Brothers, K. N. Kudin, V. N. Staroverov, R. Kobayashi, J. Normand, K. Raghavachari, A. Rendell, J. C. Burant, S. S. Iyengar, J. Tomasi, M. Cossi, N. Rega, J. M. Millam, M. Klene, J. E. Knox, J. B. Cross, V. Bakken, C. Adamo, J. Jaramillo, R. Gomperts, R. E. Stratmann, O. Yazyev, A. J. Austin, R. Cammi, C. Pomelli, J. W. Ochterski, R. L. Martin, K. Morokuma, V. G. Zakrzewski, G. A. Voth, P. Salvador, J. J. Dannenberg, S. Dapprich, A. D. Daniels, Ö. Farkas, J. B. Foresman, J. V. Ortiz, J. Cioslowski, D. J. Fox, Revision C.01; Gaussian, Inc.: Wallingford, CT, Wallingford CT, **2009**.

10.1002/chem.202004217

WILEY-VCH

FULL PAPER

Entry for the Table of Contents

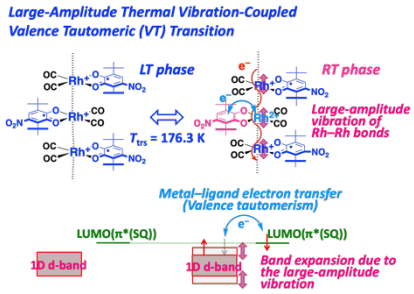

Vibronic interaction has the potential to create new fields on dynamic electronic states arising from the mixing of different electronic states by nuclear displacements. A one-dimensional rhodium–dioxolene complex undergoes drastic changes in properties with the phase transition, which are ascribable to the appearance of the mixed-valence state due to the metal–ligand electron transfer coupled with a large-amplitude vibration of Rh–Rh bonds.